Title

Excitation–inhibition balance controls coupling stability and network reorganization in a plastic Kuramoto model

Authors

Satoshi Kuroki,[1]* Kenji Mizuseki,[1]

Affiliations

[1] Department of Physiology, Osaka Metropolitan University Graduate School of Medicine, Asahimachi 1-4-3, Abeno-ku, Osaka, 545-8585, Japan

* Correspondence: skuroki@omu.ac.jp

Abstract

Sleep and rest, characterized by synchronized neuronal activity that emerges under large shifts in the excitation–inhibition balance, are crucial for synaptic reorganization in the brain. However, the network dynamics that permit rewiring without erasing stable connections remain unclear. To address this question, we extended a Kuramoto framework with excitation–inhibition balance by adding Hebbian and homeostatic plasticity. The resulting model showed that networks with robust inhibition consistently exhibited desynchronized dynamics and stable couplings. In contrast, networks with weaker inhibition exhibited a bistable regime, in which couplings of intermediate strengths fluctuated while strong couplings remained stable. These findings suggest that the dynamic interplay between network activity and plasticity selectively stabilizes stronger connections while permitting flexible reorganization of weaker ones, providing a potential mechanism for network reorganization during sleep and rest.

Introduction

Empirical evidence suggests that brain activity during sleep and rest promotes memory consolidation, knowledge abstraction, and creative insight [1,2] through the reorganization of neural circuits [3,4]. Such reorganization should rely on mechanisms distinct from those involved in learning during task performance. Indeed, synaptic plasticity during sleep and rest improves task performance [5,6].

Neuronal synchronization occurs in two distinct states. Collective neuronal firing is desynchronized during active wakefulness, including task engagement, movement, and attentional states, as well as during rapid eye movement (REM) sleep, but more synchronized during quiet wakefulness and non-REM (NREM) sleep. Throughout the paper, we refer to these regimes descriptively as wake-like/desynchronized and sleep/rest-like/synchronized or bistable states, depending on the model dynamics being discussed. The transition between these states is associated with shifts in the excitation–inhibition (EI) balance. Firing rates of inhibitory neurons and synaptic conductance of inhibitory synapses are significantly elevated during wake-like states, while those of excitatory synapses show comparatively smaller changes [7–10]. These observations raise the possibility that, during sleep/rest-like states, EI-balance-dependent changes in collective neuronal synchronization interact with synaptic plasticity to reshape network structure. However, detailed mechanisms by which neuronal synchronization in sleep/rest-like states reshapes network structure through plasticity remain unclear.

Collective synchronization of oscillators, including neurons, has been studied using coupled-oscillator models. Among these, the Kuramoto model is one of the simplest frameworks[11,12], and numerous variants have been proposed. One variant, the EI-Kuramoto model, incorporates the EI balance by dividing oscillators into excitatory and

inhibitory groups and assigning four interaction types between them[13,14]. We have previously shown that tuning these four strengths toggles the network between synchronized, desynchronized, and bistable states, potentially reflecting a neuronal synchronization mechanism[14]. That study, however, kept all coupling weights—defined in this paper as pair-specific interaction strengths—fixed and identical, and therefore could not address how EI-balance-dependent dynamical states shape synaptic coupling through plasticity over time.

In this study, we focused on Hebbian and homeostatic plasticity. Hebbian plasticity, based on the principle "fire together, wire together," strengthens synapses between neurons that fire in close temporal proximity[15]. In contrast, homeostatic plasticity regulates neuronal excitability and synaptic strength to maintain network stability, thereby preventing excessive excitation or quiescence[16]. The interplay between these plasticity mechanisms enables the emergence of diverse neuronal functions and firing patterns[17–20]. Previous studies have incorporated plasticity into Kuramoto models, enabling coupling weights to adapt based on the oscillator activity to examine their impact on system synchronization[21–31]. However, these studies focused on promoting synchronization under a single dynamic state. How distinct collective dynamics, controlled by the EI balance, differentially shape synaptic plasticity remains unexplored.

To address these gaps, we developed a plastic EI (pEI)-Kuramoto model in which excitatory–excitatory couplings undergo Hebbian potentiation and homeostatic regulation. We found that strong inhibition produced a desynchronized regime with relatively stable couplings, whereas weaker inhibition produced a bistable regime in which intermediate-strength couplings fluctuated while strong couplings remained stable. These results suggest that EI-balance-dependent collective dynamics selectively stabilize strong

74 couplings while permitting flexible reorganization of weaker ones, providing a potential
75 mechanism for network reorganization during sleep and rest.

76 **Results**

77 **Establishment of the pEI-Kuramoto model**

78 The pEI-Kuramoto model comprised two oscillator groups: excitatory units, referred to as
79 excUnits, and inhibitory units, referred to as inhUnits. These specific terms clarify that the
80 units represented excitatory and inhibitory factors in this model, rather than actual neurons
81 or synapses. Four interaction strengths were assigned between the groups, with only
82 excitatory-excitatory couplings (J_{ee}) being distributed and plastic. The other interaction
83 strengths, K_{ii} (repulsive strength between inhUnits), K_{ei} (attractive strength from excUnits
84 to inhUnits), and K_{ie} (repulsive strength from inhUnits to excUnits) were constant across
85 time and across unit pairs (Figure 1A; see Materials and Methods). The interactions are
86 modeled as zero-phase-lag sine functions. The interactions from excUnits are purely
87 attractive, while those from inhUnits are purely repulsive. Accordingly, the terms
88 "excitatory" and "inhibitory" are used synonymously with "attractive" and "repulsive,"
89 respectively.

90 First, we investigated how the distribution of pair-specific excitatory-excitatory coupling
91 weights J_{ee} affected the dynamics of the pEI-Kuramoto model in the absence of plasticity
92 (Figure 1B and C). In our previous study, we demonstrated that the Kuramoto model with
93 EI balance (EI-Kuramoto model) exhibits three distinct dynamic states—synchronized,
94 bistable, and desynchronized—depending on the balance between the constant values of
95 the interaction strengths[14]. In this study, J_{ee} followed a Gaussian distribution with a mean
96 of μ_{Jee} and a standard deviation of σ_{Jee}, where σ_{Jee} was set to 0, 1/10, and 1/2 of μ_{Jee}
97 (Figure 1B). The collective synchronization was quantified using the order parameter R,

which represents the magnitude of the average vector between the oscillator units. In this simulation, regardless of the standard deviation value, all systems with a distributed J_{ee} also exhibited synchronized (high R), bistable (alternating high and low R), and desynchronized (low R) dynamics, as observed with constant ($\sigma_{Jee} = 0$) values (Figure 1C).

Next, we incorporated plasticity into J_{ee} by applying Hebbian potentiation and homeostatic regularization plasticity rules (see Materials and Methods). Among the various methods available for implementing Hebbian plasticity in the Kuramoto model, we initially selected the simplest method: the cosine function (Figure S1A; see Materials and Methods)[21–23,26,30,31]. In this process, when a pair of excUnits exhibits closer phases, their J_{ee} coupling weight is potentiated. Simultaneously, the J_{ee} distribution was rescaled to maintain the initial mean and standard deviation, thereby preventing overpotentiation through homeostatic regularization plasticity (see Materials and Methods). The system dynamics were evaluated using the parameter set ($\mu_{Jee} = 1$, $\sigma_{Jee} = 0.1$, $K_{ei} = 3$, $K_{ie} = 3$, $K_{ii} = 3$), at which the system exhibited a desynchronized state in the absence of J_{ee} plasticity. Under the cosine rule, unit pairs with smaller phase differences acquire a larger J_{ee} weight. This rule causes the J_{ee} distribution, which was initially Gaussian, to become bimodal (Figure S1B). Plasticity also influences the distribution of oscillator units, resulting in bimodal distributions of both phase and phase difference (Figure S1C), consistent with previous studies that incorporated the Hebbian rule into the Kuramoto model[21,26]. This bimodal distribution of the coupling weight deviates from the long-tailed skewed distributions typically observed in biological synaptic weights[10,32,33].

To address this discrepancy, we introduced an exponential-based Hebbian plasticity rule to adjust the decay rate (sparseness parameter γ) of the gain for the phase difference (Figure 1D). We applied this rule to a range of parameter sets and evaluated the resulting

J_{ee} distribution using skewness, kurtosis, and dip values, which quantify the distribution bimodality[34]. Although J_{ee} distributions initially followed a Gaussian pattern, they transitioned into various bimodal or skewed forms (Figure 1E and F). We also quantified the synchronization of the excUnits using the mean and standard deviation of the order parameter R_{exc} over time, denoted as $E[R_{exc}]_t$ and $S[R_{exc}]_t$, respectively. Plasticity in J_{ee} affects synchronization (Figure 1G), resulting in uniform, bimodal, or unimodal phase and phase-difference distributions depending on the plasticity parameters (Figure S1D). Moreover, the boundary of the statistical features of the J_{ee} distribution (Figure 1E) appears to coincide with the synchronization boundary (Figure 1G). For further analysis, we chose a parameter set that resulted in a long-tailed skewed J_{ee} distribution (Figure 1F, top, magenta circle), which more closely reflects the synaptic weight distributions observed in the brain[10,32,33].

Coupling fluctuations increase in the bistable state

We next investigated how distinct dynamic states associated with different EI balances affect coupling weights. To this end, we altered the EI balance of the pEI-Kuramoto model by manipulating the interaction strength from inhUnits. We unified K_{ie} and K_{ii} into a single parameter, K_i, to simplify the simulation, following the approach used in our previous study[14]. We then examined how the J_{ee} fluctuations were associated with the K_i values, quantified as the standard deviation of J_{ee} over time ($S[J_{ee}]_t$; see Materials and Methods) (Figure 2A and B). We determined the system's dynamic state by analyzing the time course of R_{exc} (Figure 2C and D), as previously described[14].

When $K_i < 0.4$, both the average ($E\{S[J_{ee}]_t\}_n$) and standard deviation ($S\{S[J_{ee}]_t\}_n$) of $S[J_{ee}]_t$ across unit pairs were almost zero (Figure 2A and B), indicating no plastic changes in J_{ee}. In this K_i range, the system was in a synchronized state, characterized by high

$E[R_{exc}]_t$ and low $S[R_{exc}]_t$ (Figure 2C and D). The coupling weights between individual pairs exhibited no fluctuation over time after reaching the synchronized state (Figure 2E and F, K_i: 0.1; Video S1).

As K_i increased, $E\{S[J_{ee}]_t\}_n$ also increased, peaking at $K_i = 0.7$, then decreased, and eventually stabilized around $K_i = 1.5$ (Figure 2A). Meanwhile, the $S\{S[J_{ee}]_t\}_n$ continued to increase (Figure 2B). For K_i values above 1.5, the system transitioned into a desynchronized state characterized by low $E[R_{exc}]_t$ and $S[R_{exc}]_t$ values (Figure 2C and D). Strong or weak couplings remained stable over time, whereas those of intermediate strength fluctuated (Figure 2E, K_i: 1.5; Video S2). The system generated transient clusters of units coupled with strong J_{ee} weights (Figure 2F, K_i: 1.5, the lower leftmost panel, t = 24). Over time, most units left these clusters, leaving only small, stable subsets (Figure 2F, K_i: 1.5, the lower panels, t = 29–50).

In the intermediate range ($0.4 < K_i < 1.5$), the system exhibited a bistable state with high $S[R_{exc}]_t$ (Figure 2D). Notably, the $S[J_{ee}]_t$ was significantly higher in this bistable state (Figure 2A). Similar to the desynchronized state ($K_i > 1.5$), the couplings with high or low weights were stable. However, the intermediate-strength couplings fluctuated more (Figure 2E and F, K_i: 0.8 and 1.0). Notably, the number of these intermediate fluctuating couplings was higher in the intermediate K_i range (Figure 2E and F, K_i: 0.8 and 1.0; Videos S3 and S4) than in the low and high K_i ranges. Thus, transitions in the dynamic state were accompanied by changes in the coupling weight fluctuations. Particularly, the bistable state tended to exhibit larger J_{ee} fluctuations.

Note that Hebbian plasticity affected the dynamic state of the pEI-Kuramoto model (Figure S2A), slightly shifting the bifurcation points between the synchronized and bistable states, and the bistable and desynchronized states toward larger K_i values. Owing

170 to this effect, we observed a small discrepancy from the state predicted by the eigenvalue-
171 based classification for the EI-Kuramoto model[14] (data not shown). However, the overall
172 trend of the state transition from synchronized to bistable and then to desynchronized as K_i
173 values increased remained consistent across different Hebbian learning rates. The
174 enhancement of synchronization induced by Hebbian plasticity was consistent with the
175 findings of previous reports on Kuramoto models incorporating cosine-shaped Hebbian
176 plasticity[26,31]. In contrast, σ_{Jee} did not affect the dynamic states (Figure S2B), consistent
177 with the results in the absence of J_{ee} plasticity shown in Figure 1C.

178 **Intermediate couplings are selectively destabilized while the strong couplings remain**
179 **stable**

180 We further investigated coupling weight fluctuations under conditions of slightly weaker
181 inhibition than in the desynchronized state, assuming intermediate brain states between
182 wake-like and sleep/rest-like states. We analyzed the individual J_{ee} coupling weights at
183 selected points of K_i (K_i = 0.8, 1.0, and 1.5, red crosses in Figure 2A–D, except K_i = 0.1).
184 Histograms of $E[J_{ee}]_t$ (mean of J_{ee} over time for each pair of units) and $S[J_{ee}]_t$ also tended
185 to shift toward higher values as K_i decreased (Figure 3A and B). A scatter plot of $E[J_{ee}]_t$
186 and $S[J_{ee}]_t$ formed a characteristic "bow-shaped" distribution (Figure 3C). In this two-
187 dimensional distribution, data points near the minimum and maximum $E[J_{ee}]_t$ values had
188 lower $S[J_{ee}]_t$ values, whereas intermediate $E[J_{ee}]_t$ showed a higher $S[J_{ee}]_t$. This pattern was
189 consistent across all distributions for different K_i values. A similar phenomenon, the
190 stabilization of strong couplings (e.g., synapses with large mushroom-shaped spines), has
191 been observed in brain synapses[35–37].

192 Furthermore, the $S[J_{ee}]_t$ values tended to increase at intermediate $E[J_{ee}]_t$ values with
193 decreasing K_i (Figure 3C), suggesting that K_i can regulate the fluctuations in individual J_{ee}

194 plastic couplings. At high K_i values in desynchronized states (K_i = 1.5, green dots), the
195 couplings were relatively stable, whereas at low K_i values in bistable states (K_i = 1.0 and
196 0.8, orange and blue dots), the couplings of intermediate weights were more unstable.
197 Strong J_{ee} coupling remained stable with small fluctuations, even when K_i was low. These
198 dynamics may provide a mechanism that preserves the coupling of particularly strong
199 pairs and resets moderate-weight pairs, facilitating the reorganization of the network
200 structure (Figure 2E and 2F).

201 To enable a direct comparison with Figure 7A and 7B in Yasumatsu et al[37], which report
202 the relationship between spine volume and changes in spine volume in hippocampal slices,
203 we quantified the change in coupling weight, ΔJ_{ee} (= $J_{ee}(t+\Delta t) - J_{ee}(t)$), as a function of its
204 current value, J_{ee}, at each time step in our pEI-Kuramoto model (Figure 3D and E). We
205 pooled J_{ee} values and their changes ΔJ_{ee} across all excUnit pairs and time points, binned
206 the J_{ee} values, and computed the mean and the standard deviation of ΔJ_{ee} for each J_{ee} bin
207 ($E[\Delta J_{ee}]_{t,n}$ and $S[\Delta J_{ee}]_{t,n}$). In the desynchronized state (K_i = 1.5, green lines), $E[\Delta J_{ee}]_{t,n}$ was
208 slightly but significantly positive for small J_{ee} (Wilcoxon signed-rank test,
209 bin=[0.011,0.012), mean=1.1×10^{-8}, n=6,686,034, W=1.06×10^{13}, p<1.0×10^{-308}), then
210 decreased with increasing J_{ee}, reaching a local minimum near $J_{ee}\approx0.02$. Subsequently,
211 $E[\Delta J_{ee}]_{t,n}$ increased and approached zero around $J_{ee}\approx0.025$ (Figure 3D), a region
212 corresponding to the peak of $E[J_{ee}]_t$ (Figure 3A and C). $S[\Delta J_{ee}]_{t,n}$ increased monotonically
213 over the same range of J_{ee} (Figure 3E). These trends closely mirror observations in
214 hippocampal slices and *in vivo* cortical imaging[37,38]. In comparison, the bistable regimes
215 (K_i=0.8 and 1.0, orange and blue lines) showed large deviations in the mean change
216 ($E[\Delta J_{ee}]_{t,n}$) either in the same direction (K_i=1.0, orange line) or the opposite direction
217 (K_i=0.8, blue line) as the desynchronized state (Figure 3D). Furthermore, the standard

deviation ($S[\Delta J_{ee}]_{t,n}$) was generally elevated relative to the desynchronized state across the range of J_{ee} from 0.01 to 0.025 (Figure 3E).

Factors determining coupling weight properties

To identify the parameters that determine the individual J_{ee} coupling properties ($E[J_{ee}]_t$ and $S[J_{ee}]_t$) shown in Figure 3, we explored the candidate parameters (natural frequency difference $\Delta\omega$, initial phase difference $\Delta\theta$, and initial J_{ee} values of each excUnit pair) that may contribute to J_{ee} fluctuations (Figure 4). We colored the dots of $E[J_{ee}]_t$ vs. $S[J_{ee}]_t$ distribution (Figure 3C) according to each parameter value (Figure 4A–C). For statistical comparison, couplings were roughly categorized based on whether $E[J_{ee}]_t$ exceeded 0.018 (high-$E[J_{ee}]_t$ group) or not (low-$E[J_{ee}]_t$ group), because the correlation between $E[J_{ee}]_t$ and $S[J_{ee}]_t$ reversed around this point (Figure 4D–F).

Regarding differences in the natural frequency $\Delta\omega$, most pairs in the high ($\geq$0.018) $E[J_{ee}]_t$ group had relatively small $\Delta\omega$, whereas pairs with larger $\Delta\omega$ tended to be in the low (<0.018) $E[J_{ee}]_t$ group (Figure 4A and 4D). In the low-$E[J_{ee}]_t$ group, $S[J_{ee}]_t$ seemingly increased with $\Delta\omega$ (Figure 4A). The initial phase differences $\Delta\theta$ between the pairs were also significantly different between the high- and low-E $[J_{ee}]_t$ groups (Figure 4B and E). In the high-$E[J_{ee}]_t$ group, most pairs exhibited small initial $\Delta\theta$, whereas in the low-$E[J_{ee}]_t$ group, the initial $\Delta\theta$ was uniformly distributed. Additionally, we examined the effect of the initial J_{ee} coupling weight, which showed no noticeable bias (Figure 4C) and followed a normal distribution in both the high and low-$E[J_{ee}]_t$ groups (Figure 4F). Considering these results, pairs with small differences in natural frequency and initial phase positions maintained more stable and larger J_{ee} weights (Figure 4G and H). Conversely, the initial J_{ee} weight was not an important factor in determining the stability and strength of the couplings.

Theoretical analysis of quasi-steady coupling weight distribution

We investigated the theoretical mechanism underlying the fluctuation of coupling weights J_{ee} by analyzing their distribution in a quasi-steady state, assuming $J_{ee,kj}(t+\Delta t) \approx J_{ee,kj}(t)$ (Supplemental Text). Although a true static steady weight distribution does not exist in the desynchronized or bistable states due to the non-constant phases of each oscillator unit, the desynchronized condition allows for a quasi-steady state where the phase and weight distributions evolve on a sufficiently slow timescale, resulting in minimal fluctuation of the J_{ee} distribution. Under this assumption, the coupling weights do not change as a result of the plastic modulation in Equations M11 and M14, leading to the following relationship (Supplemental Text, Equation S3).

$$J_{ee,kj} = \hat{J}_{ee,kj} + c\exp\left(-\gamma\left|\Delta\theta_{kj}\right|\right) \qquad \text{(Equation 1).}$$

$$c = \frac{\alpha(1-\beta)}{\beta}$$

The first term, $\hat{J}_{ee,kj}$, represents the value of $J_{ee,kj}$, which is rescaled with the homeostatic regulation plasticity rule so that the mean and variance become $\hat{\mu}_{Jee}$ and $\hat{\sigma}_{Jee}$, respectively. The second term is the Hebbian potentiation component, scaled by the ratio between the Hebbian and homeostatic plasticity learning rates c. This equation indicates that the weight $J_{ee,kj}$ depends on the distribution of $\hat{J}_{ee,kj}$ and the distribution of phase difference between unit k and j $\Delta\theta_{kj}$ ($c\exp\left(-\gamma\left|\Delta\theta_{kj}\right|\right)$). Assuming that this rule remains applicable during the approach to a quasi-steady state, successive iterations of the update rule progressively integrate the second $\Delta\theta$-dependent Hebbian term into the J_{ee} distribution. Furthermore, the distribution of $\Delta\theta$ is dependent on that of θ (Supplemental Text). Therefore, when the weight dynamics are sufficiently slow, the J_{ee} distribution is

determined by the phase distribution. Indeed, the characteristics of the J_{ee} distribution appear to be correlated with the synchronization state of the system, which reflects the shape of the phase distribution (Figure 1E, 1F, and S1). Specifically, a uniform phase (and phase difference) distribution (desynchronized state) corresponds to a right-skewed, long-tailed J_{ee} distribution (magenta circle in Figure 1E, F and S1D). A bimodal phase distribution corresponds to a bimodal J_{ee} distribution (green circle in Figure 1E, F and S1D and the cos rule in S1B and S1C). A unimodal phase distribution (synchronized state) corresponds to a left-skewed J_{ee} distribution (yellow circle in Figure 1E, F and S1D).

Next, we considered the change in the phase difference for a pair of excUnits, $\Delta\theta_{kj}$. Assuming that $J_{ee,kj}$ and $\Delta\theta_{kj}$ are constant, the following relationship can be derived from Equations 1 and M9 (Supplemental Text, Equation S18):

$$-\Delta\omega + F_{inh} - F_{exc}^{(-kj)} = -2\left\{\hat{J}_{ee,kj} + c\exp\left(-\gamma\left|\Delta\theta_{kj}\right|\right)\right\}\sin\left(\Delta\theta_{kj}\right) \qquad \text{(Equation 2).}$$

$\Delta\omega$ is the natural frequency difference between units k and j, F_{inh} is the interaction strength from the inhUnits, and $F_{exc}^{(-kj)}$ is the interaction strength from the excUnits, except for units k and j. $F_{inh} - F_{exc}^{(-kj)}$ is the R_{exc}- and R_{inh}-dependent term; its direction can be either attractive or repulsive, depending on the phase configuration of the system (Supplemental Text). The right-hand side of this equation represents the interaction strength between units k and j, whereas the left-hand side represents the net forces of the other factors. A stable fixed point for $\Delta\theta_{kj}$ exists, where the functions for the left- and right-hand sides intersect (Figure S3).

On the right-hand side, the attractive force is driven by both the homeostatic set-point, $\hat{J}_{ee,kj}$, and the Hebbian potentiation term. Near $\Delta\theta\approx0$, the Hebbian effect is strong, yielding a large attractive force. As the phase difference $|\Delta\theta|$ increases, this Hebbian

potentiation weakens, and the coupling weight relative position within the J_{ee} distribution falls to a lower value, causing an overall attractive force reduction.

On the left-hand side, while the influence of F_{inh} and $F_{exc}^{(-kj)}$ is limited in a desynchronized state where R_{exc} and R_{inh} are near zero, their impact becomes non-negligible in the bistable state, where these order parameters undergo periodic modulation. Sufficiently large fluctuations in these forces cause the stable fixed point to disappear or be substantially displaced, thereby leading to large fluctuations in the phase difference between the unit pair.

Cyclic modulation of inhibition

Finally, we varied K_i to mimic the sleep–wake cycle[39,40]. J_{ee} fluctuated (Figure 5A, Video S5) in response to K_i modulation (Figure 5B, top panel). R_{exc} alternated between the desynchronized and bistable states (Figure 5B, middle), with corresponding changes in $\mathrm{E}\{\mathrm{S}[J_{ee}]_{\mathrm{t}}\}_{\mathrm{n}}$ (Figure 5B, bottom). When K_i was high, the system was in a desynchronized state, and $\mathrm{E}\{\mathrm{S}[J_{ee}]_{\mathrm{t}}\}_{\mathrm{n}}$ was small. Conversely, when K_i was low, the system exhibited a bistable state, and $\mathrm{E}\{\mathrm{S}[J_{ee}]_{\mathrm{t}}\}_{\mathrm{n}}$ increased. These dynamics can be considered as modeling how the circuit structure is stabilized during the wake-like state and destabilized during the sleep/rest-like state, thereby promoting circuit reorganization.

Discussion

The main conceptual advance of this study is to show that EI balance can determine not only the synchronization state of a network but also whether plastic couplings are stabilized or rendered labile. In the model, strong inhibition favored a desynchronized regime with relatively stable couplings, whereas weaker inhibition produced a bistable regime that selectively destabilized intermediate couplings while preserving the strongest

ones. This provides a candidate systems-level mechanism by which sleep/rest-like network states can promote reorganization without erasing established strong connections.

Although the sleep/rest-like state is often associated with synchrony, it is not uniformly synchronized. Near the transition between synchronized and desynchronized states, the dynamics tend to become irregular or weakly stable, as captured by two-population coupled-oscillator models [41,42]. Sleep onset can be formalized as a noisy saddle-node bifurcation [43], and macroscopic brain-state transitions are often argued to occur near the bifurcation point [44,45]. Beyond the transitions between wakefulness and sleep, even within sleep, the microarchitecture exhibits intrinsic instability, such as the NREM-REM sleep cycle[3,4,39,40], the cyclic alternating pattern in NREM sleep[46], UP–DOWN state alternations[47,48], and microarousals[49], which may reflect switching among synchronized and desynchronized states. These fluctuation-driven transitions align with the bistable regime of our model under reduced inhibition.

Preserving robust couplings while randomizing weaker ones simplifies the network, rendering it sparse. The plasticity parameters used here, which yield a long-tailed coupling-weight distribution (Figure 1E and F) similar to that observed in the brain[10,32,33] and mirror the EI balance during state transitions and in sleep/rest-like states[7–10], appear to facilitate network sparsification. The selective preservation of strong synaptic connections is also frequently observed in the brain[35–37] and is understood through molecular mechanisms, including the dynamics of NMDA receptors[5,50] and actin filaments[51]. Our results introduce a complementary, system-level mechanism for sustaining strong coupling, viewed through the dynamics of collective oscillators. Additionally, our results may be mechanistically linked to the systems-level observation that only a subset of neuronal populations remain stable while others drift[52–54]. This process resembles pruning

strategies used in artificial neural networks that facilitate knowledge generalization[55,56]. Such pruning-like dynamics are particularly relevant during sleep/rest-like states when synaptic downregulation is dominant[5,50], as fluctuations in coupling strength can weaken intermediate connections and eventually reset them toward baseline.

Fluctuations in network connectivity can promote network reorganization. In our model, bistable states under low inhibition conditions, mirroring the EI balance during state transitions and sleep/rest-like states[7–10], promoted fluctuating coupling weights between excUnits. It has also been proposed that the brain enhances neuronal circuit reorganization during the sleep/rest-like state[3,4]. Combined with mechanisms that evaluate and stabilize reorganized circuits[57]—potentially including dopaminergic signaling during NREM sleep[58], which may provide a reinforcement-like signal and gate plastic changes—the sleep/rest-like state could, in principle, contribute to the generation of novel associations, creative ideas, or innovative problem-solving strategies.

The characteristic "bow-shaped" relationship between coupling weight mean ($E[J_{ee}]_t$) and standard deviation ($S[J_{ee}]_t$) (Figure 3C) arises from the stability of phase differences between excUnits (Equation 2). Pairs with strong coupling maintain small and stable phase differences ($\Delta\theta \approx 0$), ensuring that the Hebbian potentiation term ($c \exp(-\gamma|\Delta\theta|)$) and their relative position in the J_{ee} distribution remain consistently high. In contrast, pairs with weak couplings evolve independently with fluctuations driven mainly by natural frequency differences $\Delta\omega$. The largest $S[J_{ee}]_t$ was found in pairs with intermediate weights. In this regime, the intrinsic synchronizing force between the two units is closely counterbalanced by external driving influences, chiefly their natural frequency difference, $\Delta\omega$. Furthermore, Hebbian potentiation and homeostatic depression are also balanced.

Small fluctuations in $\Delta\theta$ can frequently tip these balances and reverse the direction of the weight change, leading to large fluctuations in the coupling weight J_{ee}.

From a dynamics perspective, these mechanisms explain not only the characteristic bow-shaped distribution in Figure 3C but also a key feature of biological synapses: larger synapses are more stable than smaller ones[35–37]. Moreover, particularly in the desynchronized state, our model reproduces the relationship between synaptic size and changes in synaptic size reported in experimental studies[37,38] (Figure 3D and E, green lines; see Results), further supporting its biological relevance.

The quasi-steady J_{ee} distribution is determined by the phase-difference distribution (Figure 1E, 1F, S1C and S1D), as it reflects a transformation of the $\Delta\theta$ distribution via the Hebbian function (Equation 1). In this study, the exponential rule $c\exp\left(-\gamma\left|\Delta\theta_{kj}\right|\right)$ transforms the uniform phase-difference distribution into a hyperbolic weight distribution (Supplemental Text, Equation S8–12). Modifying the Hebbian function would allow the generation of alternative J_{ee} distributions, such as log-normal distributions commonly observed in the brain[10,32,33].

Equation 2 further predicts that unit pairs with small natural frequency differences ($\Delta\omega$) and small initial phase differences ($\Delta\theta$) are more robust and more likely to return to a stable, synchronized state even after large perturbations, consistent with the results in Figure 4. In our simulation (Figure 1F, magenta circle), the Hebbian plasticity-induced enhancement of interaction strength near $\Delta\theta$=0 is limited, even though the plasticity slightly strengthens the restoring force near the stable point (Figure S3). Thus, the tendency for pairs with small $\Delta\omega$ and small initial $\Delta\theta$ to be more robust and stable arises primarily from the underlying sinusoidal form of the baseline interaction function rather than plasticity-induced modifications. This finding resonates with experimental

observations that neurons exhibiting synchronized firing prior to learning (analogous to a small $\Delta\theta$) are preferentially incorporated into the same assembly during learning[59–61].

Fluctuations in J_{ee} at intermediate K_i levels (Figs. 2–4, K_i=0.8, 1.0) arise from bistability between synchronized and desynchronized states. This alternation perturbs phase distributions, which directly drive changes in J_{ee}. Concurrent periodic fluctuations of the order parameters R_{exc} and R_{inh} constantly modulate the interaction term, $F_{inh} - F_{exc}^{(-kj)}$ (Equation 2), further destabilizing phase differences $\Delta\theta$ of moderately coupled pairs.

While the Kuramoto model provides conceptual insight, it is substantially simpler than biological neural circuits. The model reduces neuronal interactions to attractive and repulsive forces, neglecting pulse-based communication, conduction delays, and complex network topology[62]. Additionally, our model simplifies the complexity of neuroplasticity—excluding neurotransmitters[63], inhibitory plasticity[64,65], and adaptation[66]—and does not distinguish between specific sleep stages (e.g., NREM vs. REM), which are thought to play distinct roles in memory processing and circuit reorganization[3,4]. Addressing these limitations is essential for a comprehensive understanding of neural dynamics.

Future work can extend the framework by introducing explicit evaluation and stabilization signals that select among reorganized circuits[57,67], potentially linking fluctuation-driven reorganization to selective retention during sleep and rest. Another important direction is to examine how synchrony transitions influence interregional plasticity between functionally distinct networks, such as hippocampus and cortex[68], thereby linking circuit-level reorganization to systems-level consolidation.

Materials and Methods

pEI-Kuramoto model

The original Kuramoto model[11,12,69] is expressed as:

$$\frac{d\theta_j(t)}{dt} = \omega_j + \frac{K}{N}\sum_{k}^{N} \sin\left(\theta_k(t) - \theta_j(t)\right) \qquad \text{(Equation M1)},$$

where $\theta_j(t)$ is the phase of unit j at time t, ω_j is the natural frequency of unit j following a probability distribution $g(\omega)$, N is the number of units, and K is the interaction strength among the oscillation units. In the original Kuramoto model, K is applied constantly and uniformly to all unit pairs. The order parameter R and the mean phase ψ are then calculated from the mean vector of the oscillators as:

$$Re^{i\psi} = \frac{1}{N}\sum_{j}^{N} e^{i\theta_j} \qquad \text{(Equation M2)},$$

where i denotes an imaginary unit. Given Euler's formula and Equation M2,

$$\frac{1}{N}\sum_{k}^{N} \sin(\theta_k - \theta_j) = \frac{1}{N}\sum_{k}^{N} \mathrm{Im}\left[e^{i\theta_k}e^{-i\theta_j}\right] = \mathrm{Im}\left[Re^{i\psi}e^{-i\theta_j}\right] = R\sin(\psi - \theta_j) \qquad \text{(Equation M3)}.$$

Considering Equation M3, Equation M1 becomes

$$\frac{d\theta_j}{dt} = \omega_j + KR\sin(\psi - \theta_j) \qquad \text{(Equation M4)}.$$

In our previous EI-Kuramoto model[14], the oscillation units were categorized into two groups: excitatory and inhibitory units, referred to as excUnits and inhUnits, respectively. Employing these terms clarified that the units in the model represented excitatory and inhibitory factors, distinguishing them from actual neurons or synapses. Zero-phase-lag

sine interactions are purely attractive for excUnits and purely repulsive for inhUnits. Hence, the terms "excitatory" and "inhibitory" are used interchangeably with "attractive" and "repulsive," respectively. The interaction strength K is divided into four quantifiable parameters: K_{ee} (attractive strength between excUnits), K_{ii} (repulsive strength between inhUnits), K_{ei} (attractive strength from excUnits to inhUnits), and K_{ie} (repulsive strength from inhUnits to excUnits). K_{ee}, K_{ii}, K_{ei}, and K_{ie} are distinct positive real numbers that are uniformly applicable across all the unit pairs. Consequently, Equation M4 becomes:

$$\frac{d\theta_{j,exc}}{dt} = \omega_{j,exc} + K_{ee}R_{exc}\sin\left(\psi_{exc} - \theta_{j,exc}\right) - K_{ie}R_{inh}\sin\left(\psi_{inh} - \theta_{j,exc}\right) \qquad \text{(Equation M5)}$$

for excUnits, and

$$\frac{d\theta_{j,inh}}{dt} = \omega_{j,inh} + K_{ei}R_{exc}\sin\left(\psi_{exc} - \theta_{j,inh}\right) - K_{ii}R_{inh}\sin\left(\psi_{inh} - \theta_{j,inh}\right) \qquad \text{(Equation M6)}$$

for inhUnits, where exc and inh represent the parameters for excUnits and inhUnits, respectively. The order parameter and mean phase of each excUnit and inhUnit are

$$R_{exc}e^{i\psi_{exc}} = \frac{1}{N_{exc}}\sum_{j}^{N_{exc}} e^{i\theta_{j,exc}} \qquad \text{(Equation M7)}$$

and

$$R_{inh}e^{i\psi_{inh}} = \frac{1}{N_{inh}}\sum_{j}^{N_{inh}} e^{i\theta_{j,inh}} \qquad \text{(Equation M8).}$$

In the present study, we developed a pEI-Kuramoto model (Figure 1A). A key modification of our previous EI-Kuramoto model is that the constant and uniform

interaction strength value K_{ee} is replaced with the heterogeneous and plastic coupling weight (interaction strength of an individual unit pair) matrix J_{ee}. The J_{ee} distribution is defined by its mean μ_{Jee} and standard deviation σ_{Jee}, which are scaled with the inverse of N_{exc} to adjust for the system size and to facilitate comparisons with other Kuramoto-model variants. Accordingly, the initial J_{ee} distribution follows the Gaussian distribution $g(J_{ee}) \sim \mathcal{N}(\hat{\mu}_{Jee}, (\hat{\sigma}_{Jee})^2)$, where $\hat{\mu}_{Jee} = \mu_{Jee}/\mathrm{N}_{exc}$, $\hat{\sigma}_{Jee} = \sigma_{Jee}/\mathrm{N}_{exc}$. The other interaction strengths, K_{ii}, K_{ei}, and K_{ie}, were uniform and consistently applicable across all units. Equation M5 becomes

$$\frac{d\theta_{j,exc}}{dt} = \omega_{j,exc} + \sum_{k}^{N_{exc}} J_{ee,kj} \sin\left(\theta_{k,exc} - \theta_{j,exc}\right) - K_{ie} R_{inh} \sin\left(\psi_{inh} - \theta_{j,exc}\right) \quad \text{(Equation M9).}$$

$J_{ee,kj}$ is the coupling weight between the excUnits k (pre) and j (post).

Given the rotational symmetry, when the mean natural frequencies of excUnits and inhUnits are equal, $\overline{\omega} = \overline{\omega}_{exc} = \overline{\omega}_{inh}$, they can be set to 0 rad/s, which is equivalent to rotating the coordinate frame by the mean natural frequency $\overline{\omega}$[69]. For all simulations in this study: $N_{exc} = 80$, $N_{inh} = 20$; total simulation duration $T = 50$ s; time step $dt = 0.01$ s. The $g(\omega)$ followed the Gaussian distribution $g(\omega) \sim \mathcal{N}(0, 0.01)$ for both excUnits and inhUnits. In Figs. 2–5, K_{ii} and K_{ie} are unified with the same parameter K_i to simplify the simulation.

$$K_i = K_{ie} = K_{ii} \quad \text{(Equation M10).}$$

At each time step Δt (= dt = 0.01 s in this study), the J_{ee} values were first modulated by Hebbian potentiation and then rescaled using homeostatic regularization rules. The Hebbian potentiation plasticity is implemented as an exponential function:

$$J_{Hebb} = J_{ee,kj}(t) + \alpha \exp\left(-\gamma|\Delta\theta_{kj}|\right) \qquad \text{(Equation M11).}$$

α is the learning rate for Hebbian plasticity. Note that α should scale proportionally with an inverse of N_{exc} as $\alpha \propto 1/\mathrm{N}_{exc}$ to maintain consistency across different system sizes. γ determines the sharpness of the exponential decay from the peak. $\Delta\theta_{kj}$ is the phase difference between excUnit k and j

$$\Delta\theta_{kj} = \theta_{k,exc} - \theta_{j,exc} \left(-\pi \leq \Delta\theta_{kj} < \pi\right) \qquad \text{(Equation M12).}$$

The implementation of Hebbian plasticity with a cosine function (Figure S1A) is defined as

$$J_{Hebb} = J_{ee,kj}(t) + \frac{\alpha}{2}\{\cos\left(\Delta\theta_{kj}\right) + 1\} \qquad \text{(Equation M13).}$$

In any Hebbian learning rule in this paper, weight changes of $J_{ee,kj}$ and $J_{ee,jk}$ are the same due to the symmetry with respect to the sign of $\Delta\theta_{kj}$.

After the Hebbian modulations, J_{Hebb} was rescaled with the homeostatic regularization plasticity rule to prevent overpotentiation. Plasticity was implemented as follows:

$$\hat{J}_{Hebb} = \frac{\hat{\sigma}_{Jee}}{S[J_{Hebb}]_n}(J_{Hebb} - E[J_{Hebb}]_n) + \hat{\mu}_{Jee}$$

$$J_{ee,kj}(t + \Delta t) = \beta\hat{J}_{Hebb} + (1 - \beta)J_{Hebb} \qquad \text{(Equation M14).}$$

$\hat{J}_{Hebb}$ represents the normalized value (homeostatic set-point) of J_{Hebb} under the initial setting of the mean $\hat{\mu}_{Jee}$ and standard deviation $\hat{\sigma}_{Jee}$. β is the learning rate for homeostatic plasticity. This procedure scales $J_{ee,kj}$ toward the initial targets, $\hat{\mu}_{Jee}$ and $\hat{\sigma}_{Jee}$.

The change in coupling weight at each time step ΔJ_{ee} (Figure 3D and E) was defined as

$$\Delta J_{ee} = J_{ee}(t + \Delta t) - J_{ee}(t) \qquad \text{(Equation M15)}$$

For plotting, pairs of ΔJ_{ee} and $J_{ee}(t)$ values were pooled across all excUnit pairs and time points, and the J_{ee}(t) values were binned (bin size = 0.001).

Cyclic inhibitory modulation

In Figure 5, K_i is modulated as a sine function

$$K_i = A_s \sin(\omega_s t) + C_s \qquad \text{(Equation M16)},$$

where A_s (= 0.32), ω_s (= 0.004π), and C_s (= 1.28) are the amplitude, frequency, and baseline offset for the sine modulation, respectively. The other parameters for interaction strengths are held constant to simplify the simulation: μ_{Jee} = 1, σ_{Jee} = 0.1, K_{ei} = 3, and T = 3,000 s.

Statistics

$E[\cdot]_t$ (also $E\{\cdot\}_t$) and $S[\cdot]_t$ are the mean and the standard deviation over time, respectively, where t indicates the number of time points. $E[\cdot]_n$ and $S[\cdot]_n$ are the mean and the standard deviation among unit pairs, respectively, where n indicates the number of unit pairs. $E[\cdot]_{t,n}$ and $S[\cdot]_{t,n}$ represent mean and standard deviation, respectively, pooling all values across time and unit pairs. Here, · represents a certain variable. The range of time

for the time series analyses ($E[\cdot]_t$, $S[\cdot]_t$, $E[\cdot]_{t,n}$, and $S[\cdot]_{t,n}$) is [$T/2$, T] to exclude the initial fluctuations. For Figure 5B lower panel, value of $E\{S[J_{ee}]_t\}_n$ was estimated in the time window [-15s, +15 s] for each time point.

Descriptive statistics (mean, standard deviation, kurtosis, and skewness) and statistical tests were performed using the Python NumPy and SciPy libraries. The Dip test[34] was performed using the Python Diptest Library (https://github.com/RUrlus/diptest). The dip statistic quantifies the maximum distance between the observed distribution and the closest unimodal distribution. If the data distribution is close to unimodal distribution, the dip value is low. If the distribution is bimodal, the dip value is high. Hierarchical clustering was performed using the linkage function of the Python SciPy library.

References

1. Jenkins, J.G., and Dallenbach, K.M. (1924). Obliviscence during sleep and waking. Am. J. Psychol. *35*, 605.

2. Wallas, G. (1926). The art of thought (Jonathan Cape).

3. Landmann, N., Kuhn, M., Piosczyk, H., Feige, B., Baglioni, C., Spiegelhalder, K., Frase, L., Riemann, D., Sterr, A., and Nissen, C. (2014). The reorganisation of memory during sleep. Sleep Med. Rev. *18*, 531–541.

4. Lewis, P.A., Knoblich, G., and Poe, G. (2018). How memory replay in sleep boosts creative problem-solving. Trends Cogn. Sci. *22*, 491–503.

5. Norimoto, H., Makino, K., Gao, M., Shikano, Y., Okamoto, K., Ishikawa, T., Sasaki, T., Hioki, H., Fujisawa, S., and Ikegaya, Y. (2018). Hippocampal ripples down-regulate synapses. Science *359*, 1524–1527.

6. Goto, A., Bota, A., Miya, K., Wang, J., Tsukamoto, S., Jiang, X., Hirai, D., Murayama, M., Matsuda, T., McHugh, T.J., et al. (2021). Stepwise synaptic plasticity events drive the early phase of memory consolidation. Science *374*, 857–863.

7. Haider, B., Häusser, M., and Carandini, M. (2013). Inhibition dominates sensory responses in the awake cortex. Nature *493*, 97–100.

8. Miyawaki, H., and Diba, K. (2016). Regulation of hippocampal firing by network oscillations during sleep. Curr. Biol. *26*, 893–902.

9. Alfonsa, H., Burman, R.J., Brodersen, P.J.N., Newey, S.E., Mahfooz, K., Yamagata, T., Panayi, M.C., Bannerman, D.M., Vyazovskiy, V.V., and Akerman, C.J. (2022). Intracellular chloride regulation mediates local sleep pressure in the cortex. Nat. Neurosci. *26*, 64–78.

10. Mizuseki, K., and Buzsáki, G. (2013). Preconfigured, skewed distribution of firing rates in the hippocampus and entorhinal cortex. Cell Rep. *4*, 1010–1021.

11. Kuramoto, Y. (1984). Chemical oscillations, waves, and turbulence (Springer).

12. Kuramoto, Y. (1975). Self-entrainment of a population of coupled non-linear oscillators. In International Symposium on Mathematical Problems in Theoretical Physics (Springer), pp. 420–422.

13. Montbrió, E., and Pazó, D. (2018). Kuramoto model for excitation-inhibition-based oscillations. Phys. Rev. Lett. *120*, 244101.

14. Kuroki, S., and Mizuseki, K. (2025). Excitation-inhibition balance controls synchronization in a simple model of coupled phase oscillators. Neural Comput. *37*, 1353–1372.

15. Hebb, D.O. (1949). The organization of behavior; a neuropsychological theory (Wiley).

16. Turrigiano, G.G. (2008). The self-tuning neuron: synaptic scaling of excitatory synapses. Cell *135*, 422–435.

17. Toyoizumi, T., Kaneko, M., Stryker, M.P., and Miller, K.D. (2014). Modeling the dynamic interaction of Hebbian and homeostatic plasticity. Neuron *84*, 497–510.

18. Kim, S., Jung, D., and Royer, S. (2020). Place cell maps slowly develop via competitive learning and conjunctive coding in the dentate gyrus. Nat. Commun. *11*, 4550.

19. Benas, S., Fernandez, X., and Kropff, E. (2024). Modeled grid cells aligned by a flexible attractor. eLife *12*. https://doi.org/10.7554/eLife.89851.

20. Weber, S.N., and Sprekeler, H. (2018). Learning place cells, grid cells and invariances with excitatory and inhibitory plasticity. Elife *7*, e34560.

21. Aoki, T., and Aoyagi, T. (2009). Co-evolution of phases and connection strengths in a network of phase oscillators. Phys. Rev. Lett. *102*, 034101.

22. Bronski, J.C., He, Y., Li, X., Liu, Y., Sponseller, D.R., and Wolbert, S. (2017). The stability of fixed points for a Kuramoto model with Hebbian interactions. Chaos *27*, 053110.

23. Fialkowski, J., Yanchuk, S., Sokolov, I.M., Schöll, E., Gottwald, G.A., and Berner, R. (2023). Heterogeneous nucleation in finite-size adaptive dynamical networks. Phys. Rev. Lett. *130*, 067402.

24. Ha, S.Y., Lee, J., Li, Z., and Park, J. (2018). Emergent dynamics of Kuramoto oscillators with adaptive couplings: Conservation law and fast learning. SIAM J. Appl. Dyn. Syst. *17*, 1560–1588.

25. Ha, S.Y., Noh, S.E., and Park, J. (2016). Synchronization of Kuramoto oscillators with adaptive couplings. SIAM J. Appl. Dyn. Syst. *15*, 162–194.

26. Niyogi, R.K., and English, L.Q. (2009). Learning-rate-dependent clustering and self-development in a network of coupled phase oscillators. Phys. Rev. E Stat. Nonlin. Soft Matter Phys. *80*, 066213.

27. Park, J., Poyato, D., and Soler, J. (2021). Filippov trajectories and clustering in the Kuramoto model with singular couplings. J. Eur. Math. Soc. *23*, 3193–3278.

28. Picallo, C.B., and Riecke, H. (2011). Adaptive oscillator networks with conserved overall coupling: Sequential firing and near-synchronized states. Phys. Rev. E Stat. Nonlin. Soft Matter Phys. *83*, 036206.

29. Poyato, D. (2019). Filippov flows and mean-field limits in the kinetic singular Kuramoto model. arXiv [math.AP].

30. Ren, Q., and Zhao, J. (2007). Adaptive coupling and enhanced synchronization in coupled phase oscillators. Phys. Rev. E Stat. Nonlin. Soft Matter Phys. *76*, 016207.

31. Seliger, P., Young, S.C., and Tsimring, L.S. (2002). Plasticity and learning in a network of coupled phase oscillators. Phys. Rev. E Stat. Nonlin. Soft Matter Phys. *65*, 041906.

32. Buzsáki, G., and Mizuseki, K. (2014). The log-dynamic brain: how skewed distributions affect network operations. Nat. Rev. Neurosci. *15*, 264–278.

33. Iwase, M., Diba, K., Pastalkova, E., and Mizuseki, K. (2024). Dynamics of spike transmission and suppression between principal cells and interneurons in the hippocampus and entorhinal cortex. Hippocampus *34*, 393–421.

34. Hartigan, J.A., and Hartigan, P.M. (1985). The dip test of unimodality. Ann. Stat. *13*, 70–84.

35. Holtmaat, A.J.G.D., Trachtenberg, J.T., Wilbrecht, L., Shepherd, G.M., Zhang, X., Knott, G.W., and Svoboda, K. (2005). Transient and persistent dendritic spines in the neocortex in vivo. Neuron *45*, 279–291.

36. Grutzendler, J., Kasthuri, N., and Gan, W.-B. (2002). Long-term dendritic spine stability in the adult cortex. Nature *420*, 812–816.

37. Yasumatsu, N., Matsuzaki, M., Miyazaki, T., Noguchi, J., and Kasai, H. (2008). Principles of long-term dynamics of dendritic spines. J. Neurosci. *28*, 13592–13608.

38. Loewenstein, Y., Kuras, A., and Rumpel, S. (2011). Multiplicative dynamics underlie the emergence of the log-normal distribution of spine sizes in the neocortex in vivo. J. Neurosci. *31*, 9481–9488.

39. Harris, K.D., and Thiele, A. (2011). Cortical state and attention. Nat. Rev. Neurosci. *12*, 509–523.

40. Steriade, M., and Llinás, R.R. (1988). The functional states of the thalamus and the associated neuronal interplay. Physiol. Rev. *68*, 649–742.

41. Okuda, K., and Kuramoto, Y. (1991). Mutual entrainment between populations of coupled oscillators. Progr. Theoret. Phys. *86*, 1159–1176.

42. Martens, E.A., Bick, C., and Panaggio, M.J. (2016). Chimera states in two populations with heterogeneous phase-lag. Chaos *26*, 094819.

43. Yang, D.-P., McKenzie-Sell, L., Karanjai, A., and Robinson, P.A. (2016). Wake-sleep transition as a noisy bifurcation. Phys. Rev. E. *94*, 022412.

44. Priesemann, V., Valderrama, M., Wibral, M., and Le Van Quyen, M. (2013). Neuronal avalanches differ from wakefulness to deep sleep--evidence from intracranial depth recordings in humans. PLoS Comput. Biol. *9*, e1002985.

45. Hengen, K.B., and Shew, W.L. (2025). Is criticality a unified setpoint of brain function? Neuron *113*, 2582–2598.

46. Parrino, L., Ferri, R., Bruni, O., and Terzano, M.G. (2012). Cyclic alternating pattern (CAP): the marker of sleep instability. Sleep Med. Rev. *16*, 27–45.

47. Levenstein, D., Buzsáki, G., and Rinzel, J. (2019). NREM sleep in the rodent neocortex and hippocampus reflects excitable dynamics. Nat. Commun. *10*, 2478.

48. Jercog, D., Roxin, A., Barthó, P., Luczak, A., Compte, A., and de la Rocha, J. (2017). UP-DOWN cortical dynamics reflect state transitions in a bistable network. Elife *6*. https://doi.org/10.7554/eLife.22425.

49. Lüthi, A., and Nedergaard, M. (2025). Anything but small: Microarousals stand at the crossroad between noradrenaline signaling and key sleep functions. Neuron *113*, 509–523.

50. Tononi, G., and Cirelli, C. (2020). Sleep and synaptic down-selection. Eur. J. Neurosci. *51*, 413–421.

51. Kasai, H., Hayama, T., Ishikawa, M., Watanabe, S., Yagishita, S., and Noguchi, J. (2010). Learning rules and persistence of dendritic spines. Eur. J. Neurosci. *32*, 241–249.

52. Bollmann, L., Baracskay, P., Stella, F., and Csicsvari, J. (2025). Sleep stages antagonistically modulate reactivation drift. Neuron *113*, 1446-1459.e6.

53. Ziv, Y., Burns, L.D., Cocker, E.D., Hamel, E.O., Ghosh, K.K., Kitch, L.J., El Gamal, A., and Schnitzer, M.J. (2013). Long-term dynamics of CA1 hippocampal place codes. Nat. Neurosci. *16*, 264–266.

54. Vaidya, S.P., Li, G., Chitwood, R.A., Li, Y., and Magee, J.C. (2025). Formation of an expanding memory representation in the hippocampus. Nat. Neurosci. *28*, 1510–1518.

55. Bartoldson, B., Morcos, A., Barbu, A., and Erlebacher, G. (2020). The generalization-stability tradeoff in neural network pruning. In Advances in Neural Information Processing Systems, H. Larochelle, M. Ranzato, R. Hadsell, M. F. Balcan, and H. Lin, eds. (Curran Associates, Inc.), pp. 20852–20864.

56. Hoefler, T., Alistarh, D., Ben-Nun, T., Dryden, N., and Peste, A. (2021). Sparsity in deep learning: pruning and growth for efficient inference and training in neural networks. J. Mach. Learn. Res. *22*, 10882–11005.

57. Campbell, D.T. (1960). Blind variation and selective retention in creative thought as in other knowledge processes. Psychol. Rev. *67*, 380–400.

58. Gomperts, S.N., Kloosterman, F., and Wilson, M.A. (2015). VTA neurons coordinate with the hippocampal reactivation of spatial experience. Elife *4*, e05360.

59. Dragoi, G., and Tonegawa, S. (2011). Preplay of future place cell sequences by hippocampal cellular assemblies. Nature *469*, 397–401.

60. Luczak, A., Barthó, P., and Harris, K.D. (2009). Spontaneous events outline the realm of possible sensory responses in neocortical populations. Neuron *62*, 413–425.

61. Miller, J.-E.K., Ayzenshtat, I., Carrillo-Reid, L., and Yuste, R. (2014). Visual stimuli recruit intrinsically generated cortical ensembles. Proc. Natl. Acad. Sci. U. S. A. *111*, E4053-61.

62. Izhikevich, E.M. (2010). Dynamical systems in neuroscience: The geometry of excitability and bursting (MIT Press).

63. Brzosko, Z., Mierau, S.B., and Paulsen, O. (2019). Neuromodulation of spike-timing-dependent plasticity: Past, present, and future. Neuron *103*, 563–581.

64. Wu, Y.K., Miehl, C., and Gjorgjieva, J. (2022). Regulation of circuit organization and function through inhibitory synaptic plasticity. Trends Neurosci. *45*, 884–898.

65. Chiu, C.Q., Barberis, A., and Higley, M.J. (2019). Preserving the balance: diverse forms of long-term GABAergic synaptic plasticity. Nat. Rev. Neurosci. *20*, 272–281.

66. Blitz, D.M., Foster, K.A., and Regehr, W.G. (2004). Short-term synaptic plasticity: a comparison of two synapses. Nat. Rev. Neurosci. *5*, 630–640.

67. Beaty, R.E., Benedek, M., Silvia, P.J., and Schacter, D.L. (2016). Creative cognition and brain network dynamics. Trends Cogn. Sci. *20*, 87–95.

68. Klinzing, J.G., Niethard, N., and Born, J. (2019). Mechanisms of systems memory consolidation during sleep. Nat. Neurosci. *22*, 1598–1610.

69. Acebrón, J.A., Bonilla, L.L., Pérez Vicente, C.J., Ritort, F., and Spigler, R. (2005). The Kuramoto model: A simple paradigm for synchronization phenomena. Rev. Mod. Phys. *77*, 137–185.

Acknowledgments

We would like to thank Susumu Setogawa for his insightful comments on the manuscript. This study was supported by Japan Society for the Promotion of Science KAKENHI [grant 24K18243 to S.K.; grants 23K27479 and 25H02508 to K.M.], Japan Agency for

Medical Research and Development (grant JP24wm0625216 to K.M.), and the Takeda Science Foundation [to K.M.]. The funding sources had no involvement in the study design, data collection, interpretation, or the decision to submit this paper for publication.

Author contributions:

Conceptualization: SK; Methodology: SK; Investigation: SK; Visualization: SK; Supervision: KM; Writing—original draft: SK; Writing—review & editing: SK, KM; Funding acquisition: SK, KM

Competing interests:

The authors declare that they have no known competing financial interests or personal relationships that could have appeared to influence the work reported in this paper.

Data and materials availability:

The scripts for this study can be found at Google Colaboratory: https://colab.research.google.com/drive/1v8JF97G9YdwUOh_Wuh9i_TvuGa42fLAu?usp=sharing

Figures and Tables

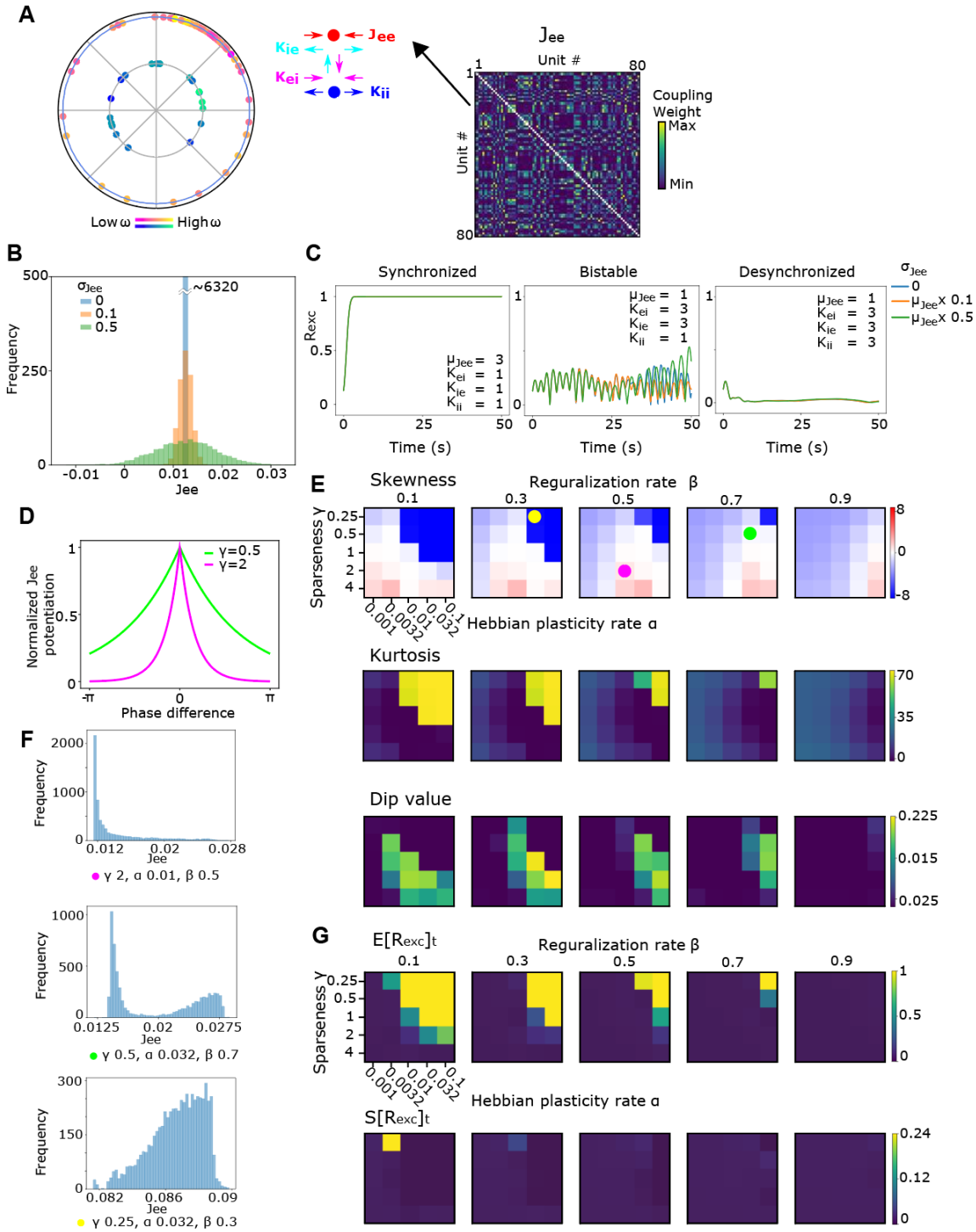

Figure 1. EI-Kuramoto model with distributed J_{ee} and plasticity. (A) Schematic representation of the pEI-Kuramoto model. Left: Oscillator units are excitatory (warm-colored) or inhibitory (cool-colored), each with its own natural frequency

(shown by color gradients). Middle: J_{ee} functions attractively between excUnits (red arrows). K_{ei} is the attractive interaction strength from excUnit to inhUnit (magenta arrow). K_{ii} represents the repulsive strength between inhUnits (blue arrows). K_{ie} is the repulsive strength from inhUnit to excUnit (cyan arrow). K_{ei}, K_{ii}, and K_{ie} are constants that are applied uniformly across all units. Right: Each J_{ee} unit pair has its own coupling weight and undergoes plastic modification. (B) Distribution of J_{ee} coupling weights with different σ_{Jee}. $\mu_{Jee} = 1$, $N_{exc} = 80$. (C) R_{exc} time traces of synchronized, bistable, and desynchronized states with each σ_{Jee} and no plasticity. (D) Exponential rules of Hebbian potentiation plasticity. The J_{ee} weight of each pair of units is potentiated based on the phase difference between the units. (E) Evaluation of the J_{ee} distribution at the last frame ($t = 50$ s) with various plasticity parameters. Skewness (top panels), kurtosis (middle), and dip values (bottom). (F) J_{ee} distribution of exponential Hebbian plasticity rules at the last frame ($t = 50$ s) with various parameter settings. The parameter settings of the top, middle, and bottom panels correspond to those marked by magenta, green, and yellow circles in (E). (G) Evaluation of state synchrony with various plasticity parameters. $\mathrm{E}[R_{exc}]_t$ and $\mathrm{S}[R_{exc}]_t$ denote the time-averaged mean and standard deviation, respectively, of the order parameter for excUnits, R_{exc}. The parameters used for evaluation were $N_{exc} = 80$, $N_{inh} = 20$, $\mu_{Jee} = 1$, $\sigma_{Jee} = 0.1$, $K_{ei} = 3$, $K_{ie} = 3$, $K_{ii} = 3$, corresponding to a desynchronized state of the system without plasticity (E–G).

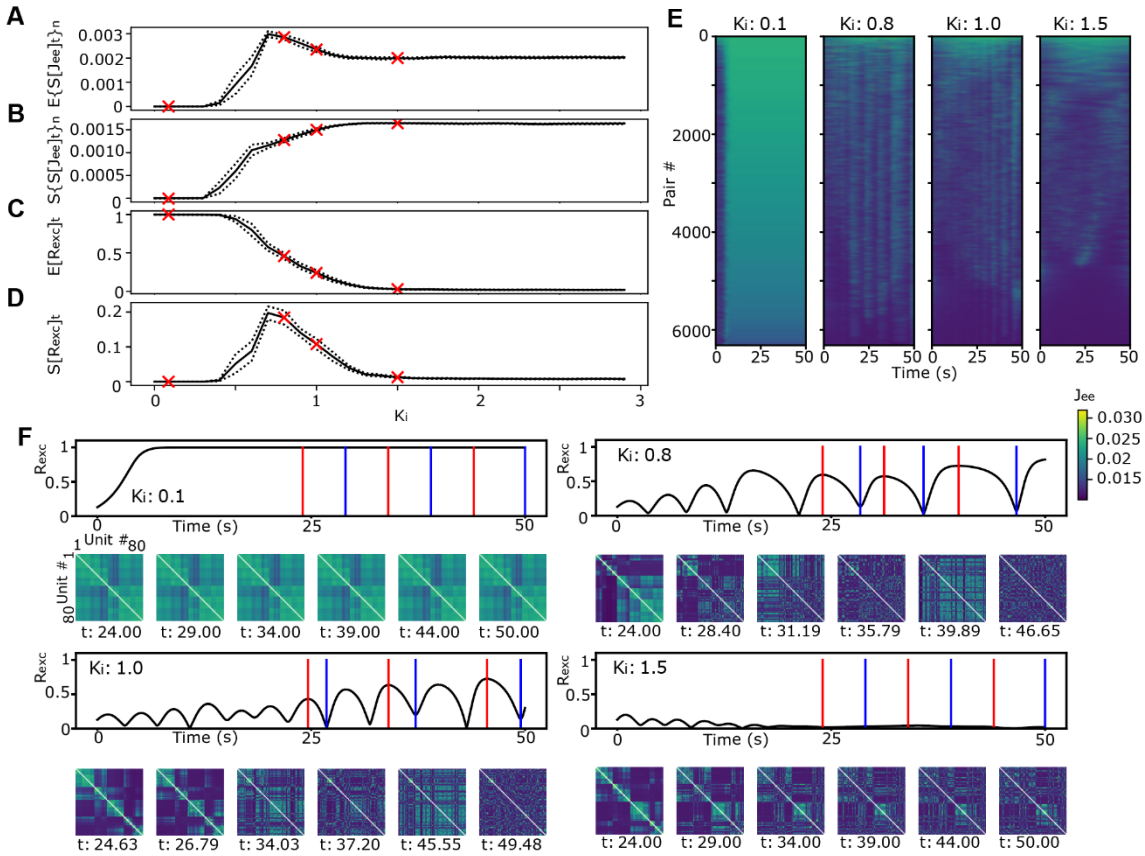

Figure 2. Changes in J_{ee} fluctuation with K_i modification. (A–D) (A) $E\{S[J_{ee}]_t\}_n$, (B) $S\{S[J_{ee}]_t\}_n$, (C) $E[R_{exc}]_t$, and (D) $S[R_{exc}]_t$ as a function of K_i. Red crosses indicate each value in the K_i conditions shown in (E) and (F). (E) Time course of J_{ee} weights under different K_i conditions. The order of unit pairs is sorted by $E[J_{ee}]_t$ for each K_i value. (F) Upper panels show R_{exc} traces. The lower panels show the J_{ee} weight matrix at selected time points indicated by the red and blue vertical lines in the top panels (red and blue are local maximum and local minimum, respectively, for $K_i = 0.8$ and 1.0; $t = 24$, 29, 34, 39, 44, and 50 for $K_i = 0.1$ and 1.5). The order of units is rearranged by the result of hierarchical clustering for the leftmost panel (around t: 24-25). E and F share the color bar. $\mu_{Jee} = 1$, $\sigma_{Jee} = 0.1$, $K_{ei} = 3$, $\alpha = 0.01$, $\beta = 0.5$, $\gamma = 2$.

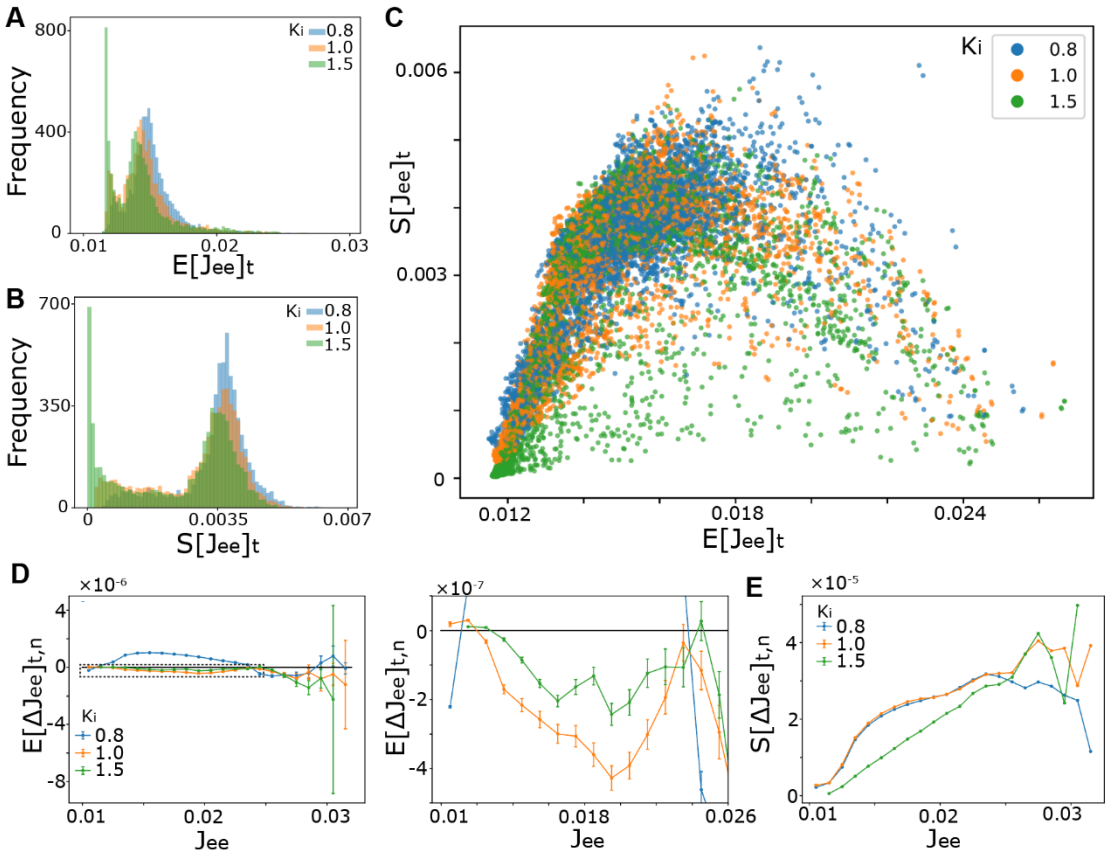

Figure 3. Relationship between the magnitude and fluctuation of J_{ee}. (A) $E[J_{ee}]_t$ histogram. (B) $S[J_{ee}]_t$ histogram. (C) $E[J_{ee}]_t$ vs. $S[J_{ee}]_t$ scatter plot for different K_i values. (D) $E[\Delta J_{ee}]_{t,n}$ as a function of J_{ee} for different K_i values. The right panel shows an enlarged view of the region enclosed by the dotted rectangle in the left panel. Black line indicates $E[\Delta J_{ee}]_{t,n} = 0$. Error bars indicate the standard error of the mean (SEM). (E) $S[\Delta J_{ee}]_{t,n}$ as a function of J_{ee} for different K_i values. At each time point, all pairs of ΔJ_{ee} and the immediately preceding J_{ee} values were collected, binned by the J_{ee} values, and used to compute the statistics within each bin (D, E). $\mu_{Jee} = 1$, $\sigma_{Jee} = 0.1$, $K_{ei} = 3$, $\alpha = 0.01$, $\beta = 0.5$, $\gamma = 2$.

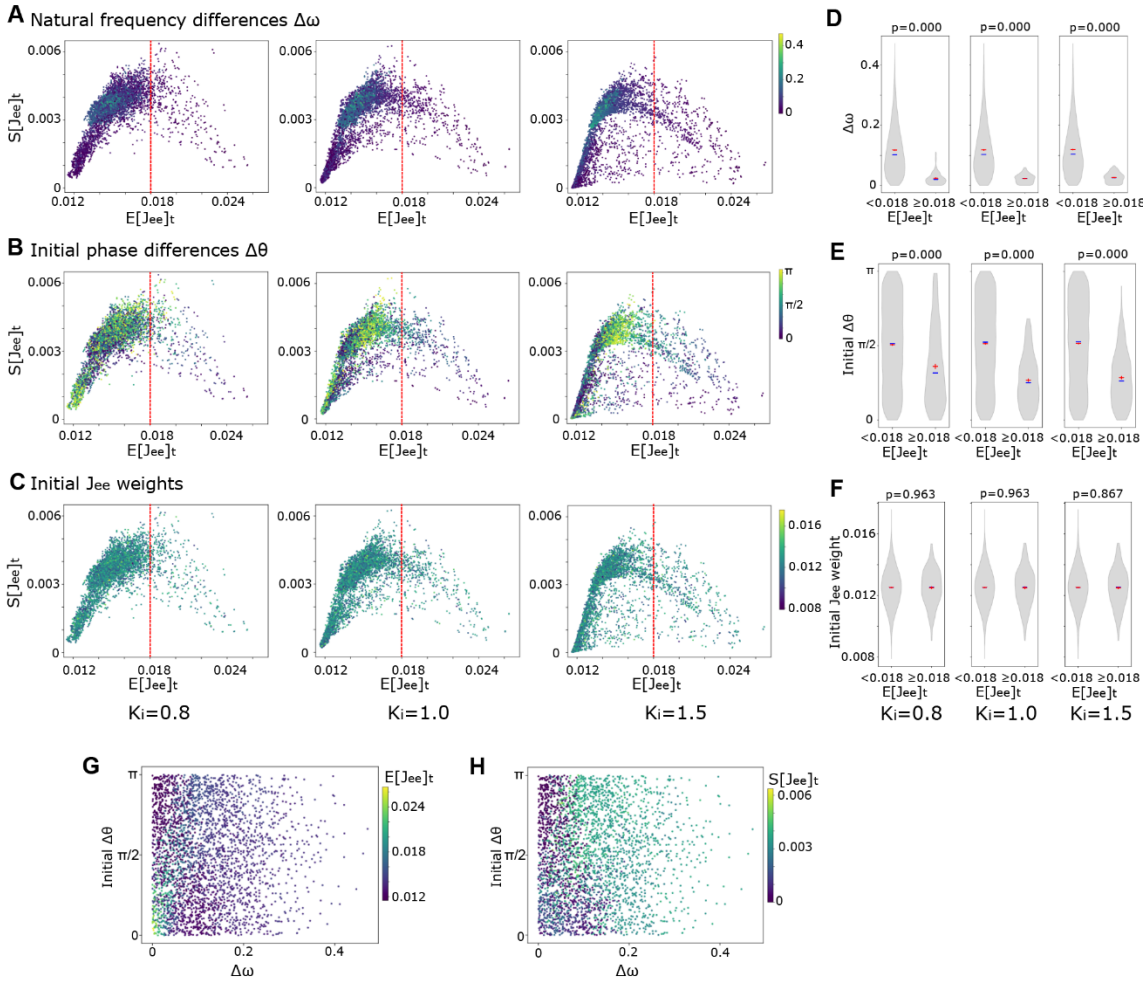

Figure 4. Factors affecting the J_{ee} fluctuation. (A–C) E[J_{ee}]$_t$ vs. S[J_{ee}]$_t$ scatter plot with color coding of (A) the natural frequency difference $\Delta\omega$, (B) the initial phase difference $\Delta\theta$, and (C) the initial J_{ee} weight over different K_i. The red dotted line for each panel indicates E[J_{ee}]$_t$ = 0.018. Left column, K_i = 0.8; middle column, K_i = 1.0; right column, K_i = 1.5. (D–F) Violin plots provide distribution densities based on whether the threshold E[J_{ee}]$_t$ ≥ 0.18 or not for (D) natural frequency differences $\Delta\omega$, (E) initial phase differences $\Delta\theta$, and (F) initial J_{ee} weights across different K_i. The red and blue horizontal lines indicate the mean and median values, respectively. The red vertical lines indicate the standard errors. The numbers in the upper right corner of each panel are the p-values from the Mann–Whitney U-test. The numbers of unit pairs were as follows: for K_i = 0.8, E[J_{ee}]$_t$ < 0.018: n = 5,968, E[J_{ee}]$_t$ ≥ 0.018: n = 352; for K_i = 1.0, E[J_{ee}]$_t$ < 0.018: n = 5,920, E[J_{ee}]$_t$ ≥ 0.018: n =

400; for $K_i = 1.5$, $E[J_{ee}]_t < 0.018$: $n = 5{,}852$, $E[J_{ee}]_t \geq 0.018$: $n = 468$. The statistics were as follows: (D, natural frequency difference), $K_i = 0.8$, $z = 24.7$, $p < 0.001$; $K_i = 1.0$, $z = 26.8$, $p < 0.001$; $K_i = 1.5$, $z = 27.8$, $p < 0.001$. (E, initial phase difference) $K_i = 0.8$, $z = 9.20$, $p < 0.001$; $K_i = 1.0$, $z = 16.4$, $p < 0.001$; $K_i = 1.5$, $z = 16.7$, $p < 0.001$. (F, initial J_{ee} weight) $K_i = 0.8$, $z = -0.046$, $p = 0.96$; $K_i = 1.0$, $z = 0.046$, $p = 0.96$; $K_i = 1.5$, $z = 0.17$, $p = 0.87$. (G and H) Scatter plots of natural frequency differences $\Delta\omega$ and initial phase differences $\Delta\theta$ with color coding of (G) $E[J_{ee}]_t$ and (H) $S[J_{ee}]_t$ ($K_i = 1.5$). $\mu_{Jee} = 1$, $\sigma_{Jee} = 0.1$, $K_{ei} = 3$, $\alpha = 0.01$, $\beta = 0.5$, $\gamma = 2$.

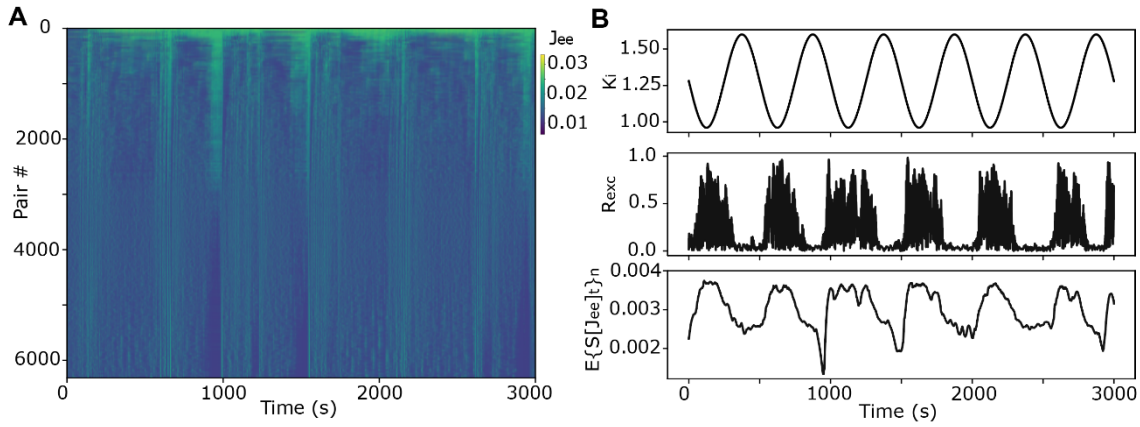

Figure 5. J_{ee} fluctuation changes with K_i cyclic modulation. (A) Time trace of each J_{ee} weight sorted by $E[J_{ee}]_t$. (B) Time traces of (top) K_i modulation, (middle) R_{exc}, and (low) $E\{S[J_{ee}]_t\}_n$. $\mu_{Jee} = 1$, $\sigma_{Jee} = 0.1$, $K_{ei} = 3$, $\alpha = 0.01$, $\beta = 0.5$, $\gamma = 2$.

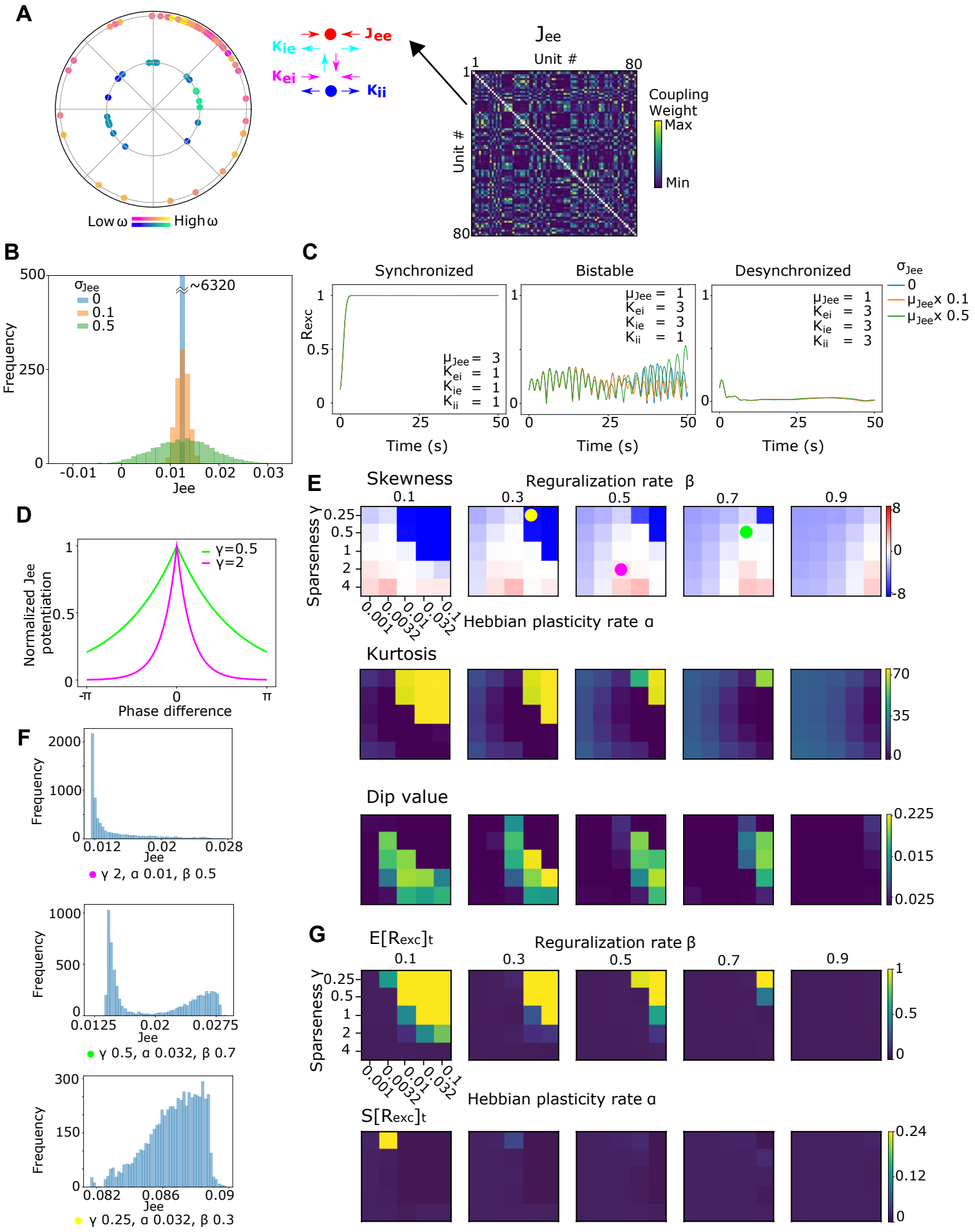
A
Low ω
High ω
Kie
Jee
Kei
Kii
Jee
Unit #
1
80
Coupling Weight
Max
Min
B
Frequency
σJee
0
0.1
0.5
~6320
Jee
C
Synchronized
Bistable
Desynchronized
Rexc
Time (s)
μJee = 3
Kei = 1
Kie = 1
Kii = 1
μJee = 1
Kei = 3
Kie = 3
Kii = 1
μJee = 1
Kei = 3
Kie = 3
Kii = 3
σJee
0
μJee x 0.1
μJee x 0.5
D
Normalized Jee potentiation
γ=0.5
γ=2
Phase difference
E
Skewness
Reguralization rate β
Sparseness γ
Hebbian plasticity rate α
Kurtosis
Dip value
F
Frequency
Jee
γ 2, α 0.01, β 0.5
γ 0.5, α 0.032, β 0.7
γ 0.25, α 0.032, β 0.3
G
E[Rexc]t
S[Rexc]t

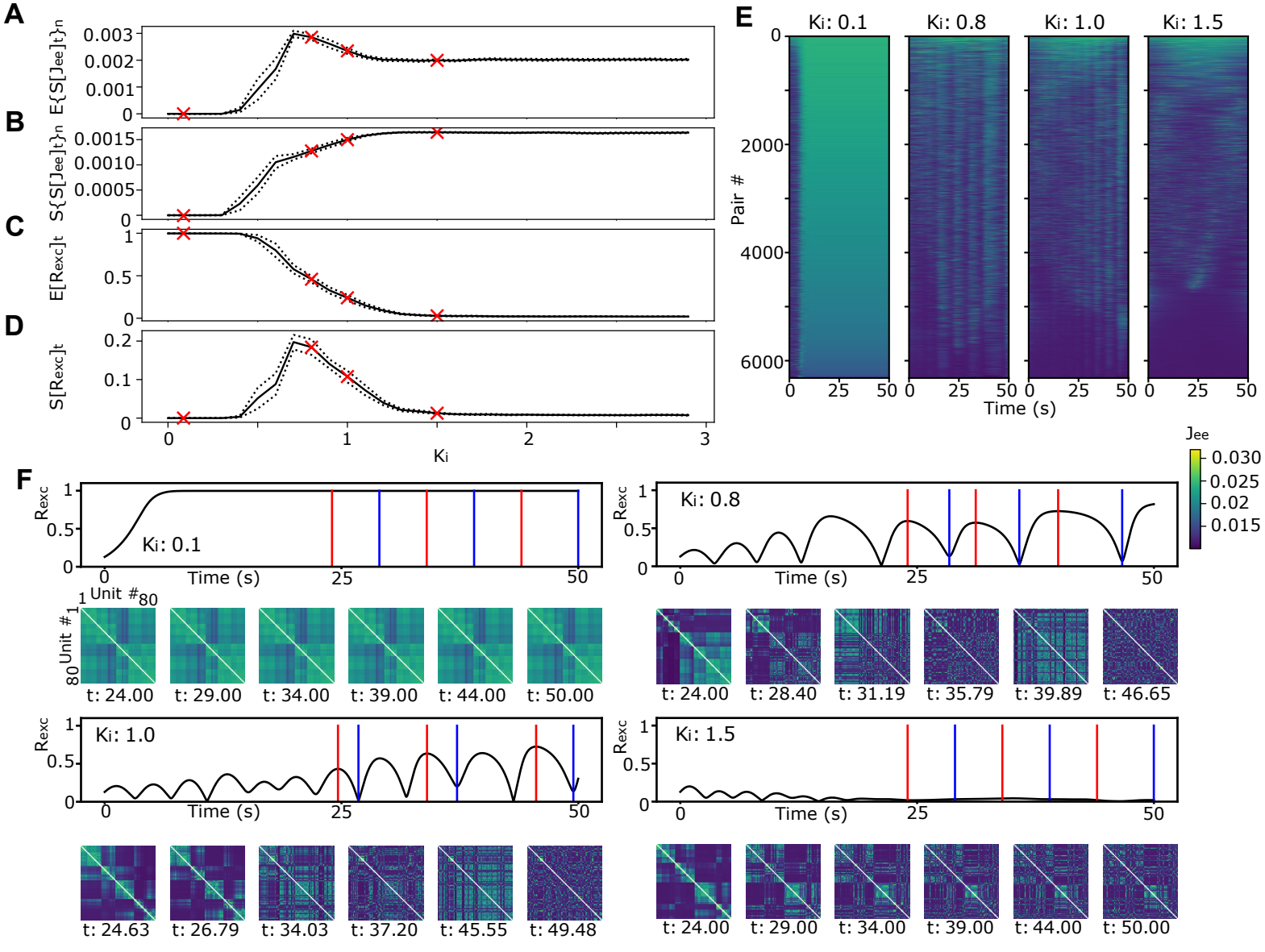
A
E{S[Jee]t}n
0.003
0.002
0.001
0
B
S{S[Jee]t}n
0.0015
0.0010
0.0005
0
C
E[Rexc]t
1
0.5
0
D
S[Rexc]t
0.2
0.1
0
0
1
2
3
Ki
E
Ki: 0.1
Ki: 0.8
Ki: 1.0
Ki: 1.5
Pair #
0
2000
4000
6000
0
25
50
Time (s)
Jee
0.030
0.025
0.02
0.015
F
Rexc
Ki: 0.1
Time (s)
Unit #
1
80
t: 24.00
t: 29.00
t: 34.00
t: 39.00
t: 44.00
t: 50.00
Ki: 0.8
t: 24.00
t: 28.40
t: 31.19
t: 35.79
t: 39.89
t: 46.65
Ki: 1.0
t: 24.63
t: 26.79
t: 34.03
t: 37.20
t: 45.55
t: 49.48
Ki: 1.5
t: 24.00
t: 29.00
t: 34.00
t: 39.00
t: 44.00
t: 50.00

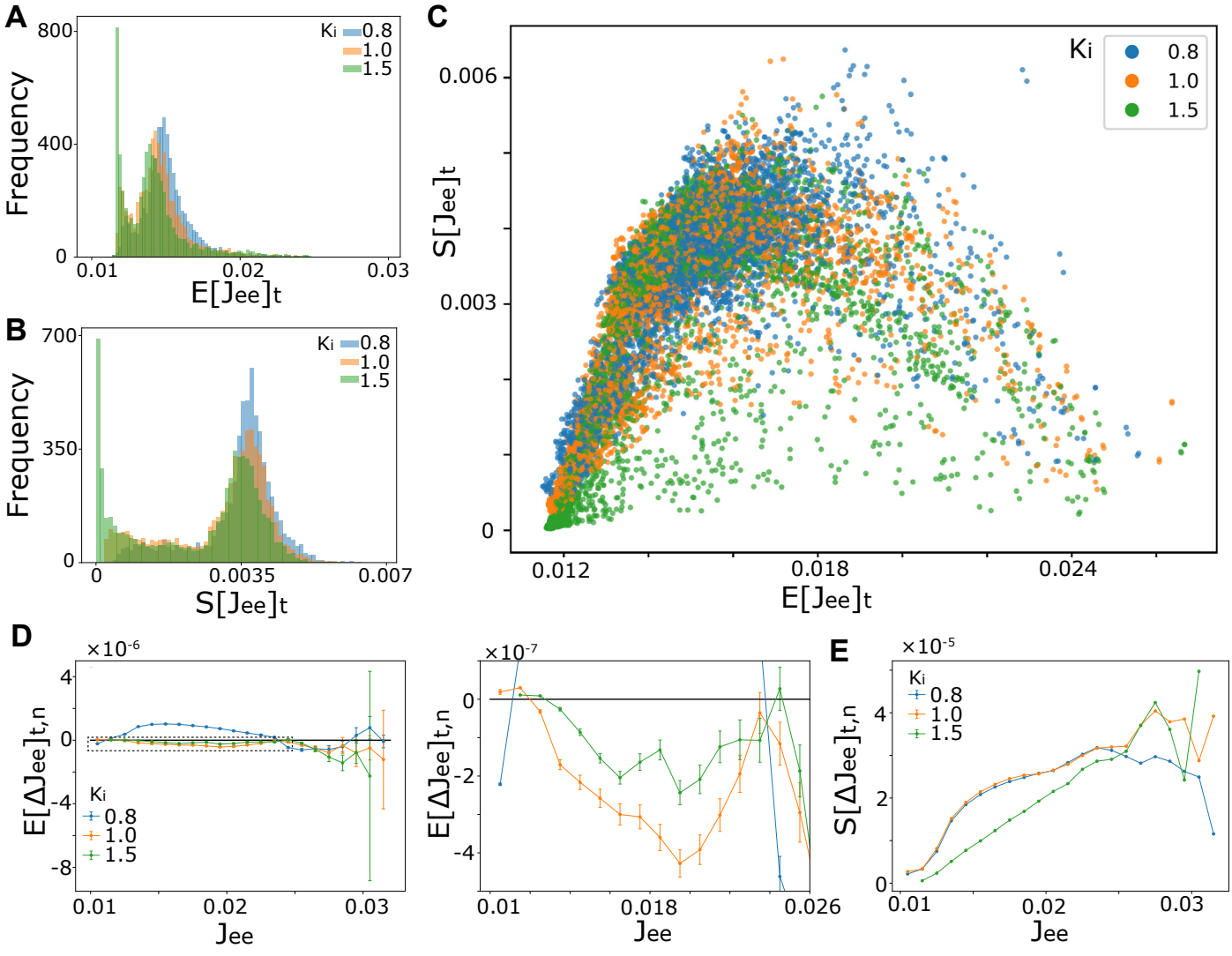
A
Frequency
E[Jee]t
Ki
0.8
1.0
1.5
B
Frequency
S[Jee]t
C
S[Jee]t
E[Jee]t
D
E[ΔJee]t,n
Jee
E
S[ΔJee]t,n

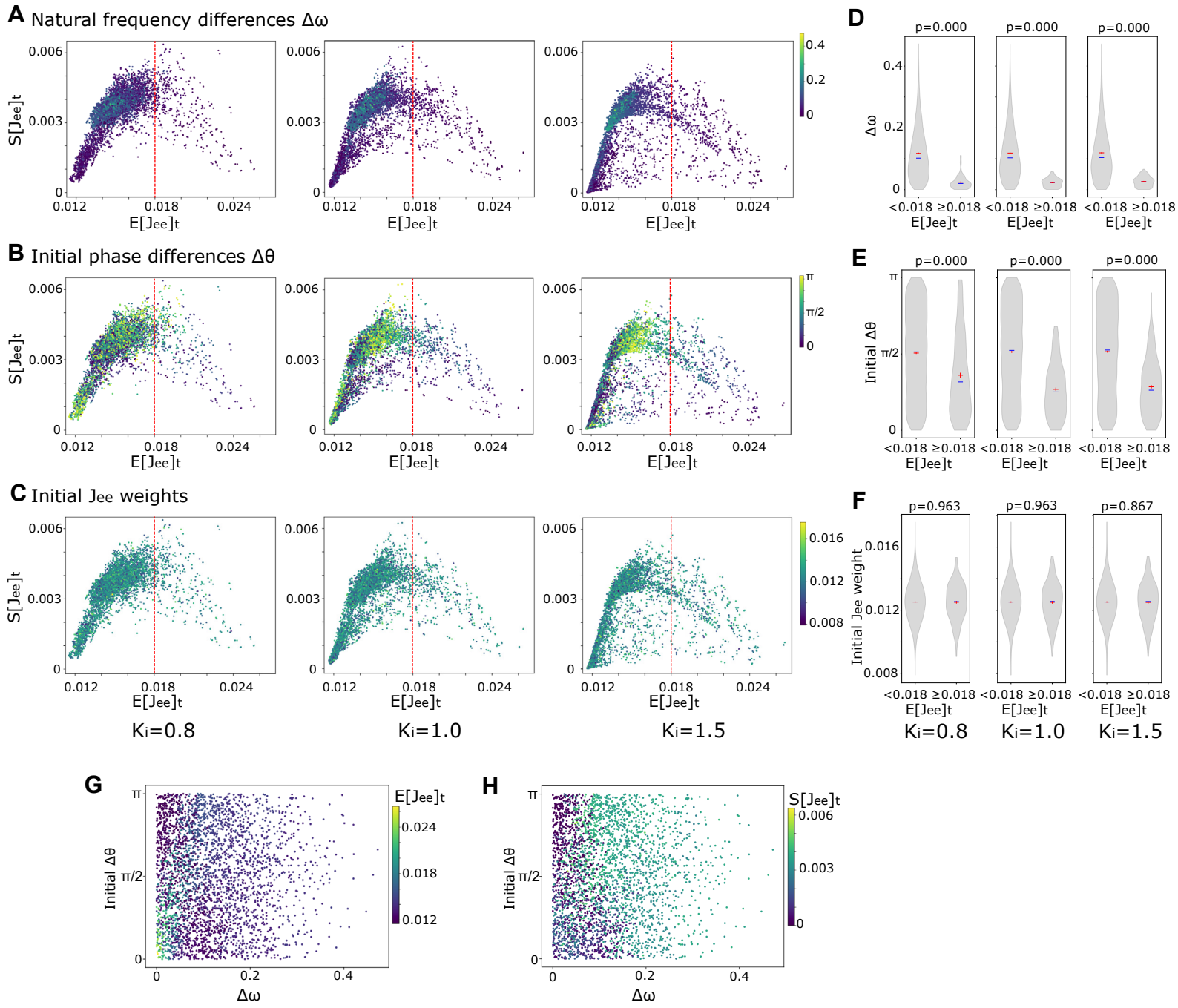
A Natural frequency differences Δω
B Initial phase differences Δθ
C Initial Jee weights
S[Jee]t
E[Jee]t
Ki=0.8
Ki=1.0
Ki=1.5
D
E
F
p=0.000
p=0.963
p=0.867
Δω
Initial Δθ
Initial Jee weight
<0.018 ≥0.018
G
H
Initial Δθ
Δω
E[Jee]t
S[Jee]t

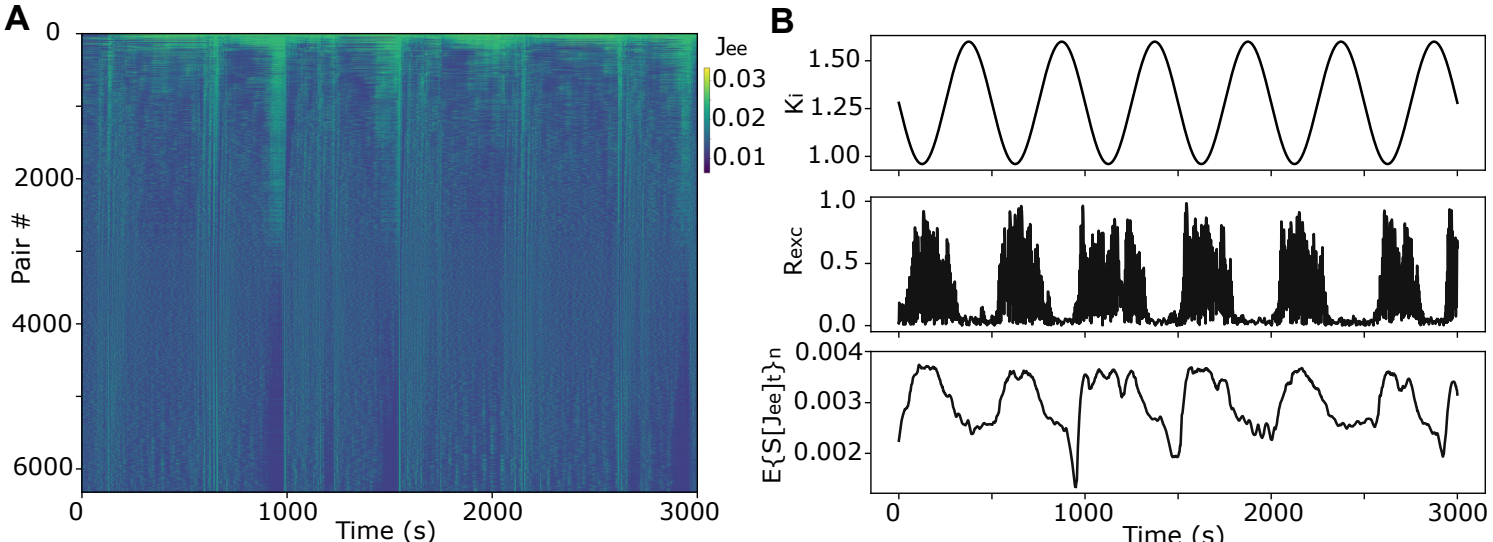
A
0
2000
4000
6000
Pair #
0
1000
2000
3000
Time (s)
Jee
0.03
0.02
0.01
B
1.50
1.25
1.00
Ki
1.0
0.5
0.0
Rexc
0.004
0.003
0.002
E{S[Jee]t}n
0
1000
2000
3000
Time (s)